IEEE Access
Multidisciplinary | Rapid Review | Open Access Journal

Received 1 September 2022, accepted 25 September 2022, date of publication 4 October 2022, date of current version 11 October 2022.

*Digital Object Identifier 10.1109/ACCESS.2022.3211951*

RESEARCH ARTICLE

# Finite-Difference-Impedance Method for Time-Delay Systems

**JUAN SEGUNDO-RAMÍREZ, (Member, IEEE), JULIO HERNÁNDEZ-RAMÍREZ, NANCY VISAIRO-CRUZ, (Member, IEEE), AND C. ALBERTO NÚÑEZ GUITIÉRREZ**
CIEP, Facultad de Ingeniería, Universidad Autónoma de San Luis Potosí, San Luis Potosí 78290, Mexico

Corresponding author: Julio Hernández-Ramírez (jarmonyhr@gmail.com)

This work was supported in part by the Consejo Nacional de Ciencia y Tecnología (CONACYT) under Grant 746757, and in part by Project FORDECYT-PRONACES/1311344/2020.

**ABSTRACT** The stability issues assessment by the impedance-based method demands the computation of accurate small-signal models. However, obtaining impedance models can be a time-consuming task if analytical models or the perturbation-based method are used. Especially in large-scale, poorly damped, distributed, and frequency-dependent parameter systems. A third approach, which has been less explored, is based on numerical derivative approximations, rather than analytical equations or time-domain simulations. This approach works with large-scale systems, avoiding tedious mathematical expressions and large recursive time-domain simulations. As a step-forward in this approach, this paper proposes a numerical-oriented method, based on the finite-difference method, to compute impedance models of time-delay power-electronics-based power systems. An outstanding feature of the proposal is the capability to incorporate the exact delays into the numerical models of impedance without resorting to approximations nor increasing the size of the system model. We compare the proposed method with the analytical and perturbation methods using a grid-connected microgrid with two power electronic inverters as a test system. The results confirm the correct performance of the proposal.

**INDEX TERMS** Impedance-based method, small-signal stability, VSC-based systems, time-delay.

## I. INTRODUCTION

The impedance based stability method [1] has been considered as a tool that provides valuable information related to the small-signal stability and performance of the port-interactions in power systems with power electronics penetration around steady-state operating points. Systems based on power converters have been analyzed with impedance models in several reference frameworks, such as wind farms type III and IV along with high voltage direct current (HVDC) transmission systems based on line-commuted converters (LCC) or voltage source converters (VSC) [2], [3] were modeled with sequence impedance. Similarly, the effect of inertial support techniques in the sequence impedance models is studied in [4] and [5]. The *DQ* framework is used to study HVDC-VSC systems, power converters and microgrids [6], [7], [8], [9], [10]. Impedance models of modular multi-level converters (MMC) are commonly derived in the harmonic state space (HSS) to preserve the harmonic coupling in these converters [11], [12], [13], [14]. Other proposals have been presented as the $\alpha\beta$-domain [15], [16] and the modified sequence domain [17], [18], [19]. Regardless of the selected framework, the impedance models are got by either analytic procedures or applying successive small perturbations at different frequencies of interest. The former option is commonly preferred because of the following reasons: provides accurate insights of the interactions between the subsystems, leads to closed expressions, the exact effect of every parameter in the small-signal models can be measured, helps to reinforce the knowledge related to small-signal issues, among others. Deriving impedance models with the analytical method can be an overwhelming work, especially for large-scale systems. On the other hand, the perturbation method [20] works with measurements of voltages and currents at the terminals of subsystems; measurements come from real systems or simulations. Regarding to this, several approaches have been used

The associate editor coordinating the review of this manuscript and approving it for publication was Meng Huang.

to identify the impedance models injecting a small amplitude signal at the point of interaction, where the subsystems need to be identified. The injection corresponds to three phase voltages (series) or currents (shunt) [21], [22] or single phase perturbations [23]. These examples use a single-tone procedure, applying the perturbation at different frequencies one by one, which can be a slow procedure.

On the other hand, the approach based on pseudo-random-sequence (PRS) perturbations can be a faster option to identify the impedance. Typical signals are the binary, near-binary and non-binary sequences, with binary being preferred for identification applications in power electronics [24]. Popular alternatives among the binary sequences are the maximum-length pseudo random binary (MLBS), the inverse-repeat binary (IRS), the discrete-interval binary (DIBS) and orthogonal binary sequences [25], [26], [27]. Another method to determine the impedance applies changes in the references of the active or reactive power in the power electronics control [28]. This technique originally uses measured information of the system when operates in two conditions; however, there has been alternatives that uses three [29] or four operating points [30] in order to estimate the impedance. Employing more measured points can improve the accuracy of the estimation, and reduces the effect of the inherent coupling in the *dq* framework [31]. On the other hand, a novel approach using artificial neural networks to identify impedance under several operating conditions is presented in [32]. In most of the reported works devoted to the small-signal stability analysis present the identification impedance as a backup to validate the analytic models, although the intrinsic practical approach of this method lead to its application in real systems as is reported in [33].

A third alternative little addressed is the numerical approaches that seek to avoid the analytical work that represents the linearization of the nonlinear model and algebraic manipulation. The usage of built-in functions of MATLAB is used in [34] to linearized models implemented in SIMULINK; an iterative algorithm is used in [35] to identify the impedance; in both works, the impedance is computed using the *DQ* framework. The periodic small-signal analysis (PAC) is presented in [36] to numerically derived impedance models of an MMC-VSC, then the vector fitting is used to compute analytical transfer functions. The numeric approach is not restricted to the impedance models, in [37] is presented a methodology to derive a state space model of electronic converters in the extended harmonic domain (EHD) using a forward finite difference approximation. In this regards, a previous work of the authors has introduced the so-called finite-difference-impedance method (FDIM) where the forward finite-difference approximation [38] is used to compute a linear time invariant (LTI) model, and afterward the impedance models are determined using a systematic procedure. The method is oriented toward systems modeled in *DQ*-domain, and its outstanding features are the generality to compute the impedance of large systems, it does not matter the control techniques (linear/nonlinear), it takes less time to get the impedance compared to the analytic or the perturbation approach, and its accuracy is much better that the perturbation approach. Nonetheless, [38] needs the ordinary differential equations (ODEs) system, which leads to approximate the delays with rational functions. However, incorporate the delay in this manner may lead to a deficient model to assess stability because of high frequency dynamics are overlooked; this is vital to understand the harmonic stability issues related to power electronics, whose behaviour exhibits non-passive properties in this frequency range related to time-delayed [39]. Despite the order of the approximation can be increased to improve its performance, this turns out in a higher-order model. So, it is better trying to represent the delay exactly. Motivated by this issue, the aim of the present work is to introduce a procedure to incorporate the delays into the finite-difference-impedance method in an exact form without increasing the system order. This extension complements the previous proposal and opens the possibility of exploring hybrid approaches, where parts can be numerically or analytically computed.

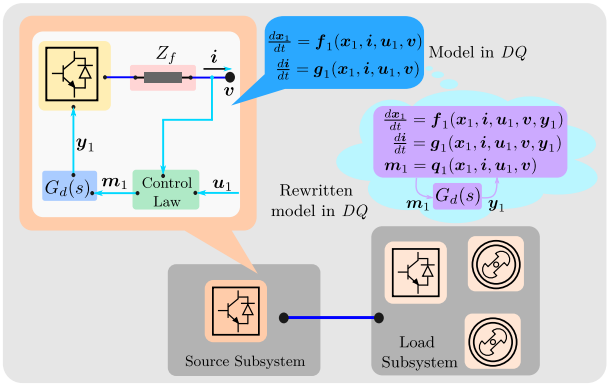


**FIGURE 1.** Separation of the subsystems.

The structure of this document is: section II explains the proposal to add the delay to the finite-difference-impedance method that can be seen as an extension of the original FDIM, but with an analytical term. In section III, the proposal is compared with the analytical and perturbation approaches; it is also shown the application of the numerical Laplace transform to obtain time-domain responses from the impedance models and the generalized Nyquist stability criterion (GNSC) to assess small-signal stability. Finally, in section IV the conclusions are given.

## II. FORMULATION OF THE ANALYTIC EXTENSION

Let us consider a system that is divided as Figure 1 shows. Here, the source subsystem will be represented just as a power electronic converter with closed-loop control; however, many more devices components can be included. The source subsystem has its average model in *DQ* as [38]:

$$\frac{d\boldsymbol{x}_1}{dt} = \boldsymbol{f}_1(\boldsymbol{x}_1, \boldsymbol{i}, \boldsymbol{u}_1, \boldsymbol{v})$$

$$\frac{d\boldsymbol{i}}{dt} = \boldsymbol{g}_1(\boldsymbol{x}_1, \boldsymbol{i}, \boldsymbol{u}_1, \boldsymbol{v}) \tag{1}$$

Hereinafter, lower case bold fonts indicate vector variables, then $\boldsymbol{x}_1$ is for the state vector related to elements of the source subsystem, $\boldsymbol{u}_1$ represents the control references, the current $\boldsymbol{i}$ and the voltage $\boldsymbol{v}$ in the interface are also explicitly shown in the ODE set. There is a passive filter (whose topology can be whatsoever) in terminals of the converter that is represented by the element $Z_f$. It is worth noting that the control strategy takes the control reference $\boldsymbol{u}_1$, and the voltage and current $\boldsymbol{v}, \boldsymbol{i}$ as inputs, and gives as output the modulation $\boldsymbol{m}_1$. Then, the effect of the PWM causes that a delayed modulation $\boldsymbol{y}_1$ be applied to the converter. In (1), the delay dynamics are included in $\boldsymbol{x}_1$ and in the vector field $\boldsymbol{f}_1()$; however, it is observed that a relationship between $\boldsymbol{m}_1$ (which results of algebraic operations $\boldsymbol{m}_1 = \boldsymbol{q}_1(\boldsymbol{x}_1, \boldsymbol{i}, \boldsymbol{u}_1, \boldsymbol{v})$), and $\boldsymbol{y}_1$ is always held, this can be written in the frequency domain as a linear relationship:

$$\boldsymbol{Y}_1(s) = G_d(s)\boldsymbol{M}_1(s) \tag{2}$$

where $G_d(s)$ is the delay transfer function. If $G_d(s) = e^{-T_s s}$, the pure delay is incorporated into the model, but in this case it is not possible to get an ODE set (2), unless to resort to delay differential equations. Now, $\boldsymbol{y}_1$ is considered as a new input and (1) is rewritten as follows:

$$\begin{aligned} \frac{d\boldsymbol{x}_1}{dt} &= \boldsymbol{f}_1(\boldsymbol{x}_1, \boldsymbol{i}, \boldsymbol{u}_1, \boldsymbol{v}, \boldsymbol{y}_1) \\ \frac{d\boldsymbol{i}}{dt} &= \boldsymbol{g}_1(\boldsymbol{x}_1, \boldsymbol{i}, \boldsymbol{u}_1, \boldsymbol{v}, \boldsymbol{y}_1) \\ \boldsymbol{m}_1 &= \boldsymbol{q}_1(\boldsymbol{x}_1, \boldsymbol{i}, \boldsymbol{u}_1, \boldsymbol{v}) \end{aligned} \tag{3}$$

Around the steady-state operating point $(\boldsymbol{x}_1^0, \boldsymbol{i}^0, \boldsymbol{v}^0, \boldsymbol{y}_1^0)$, the following small-signal model is obtained:

$$\begin{aligned} \frac{d}{dt}\begin{bmatrix}\Delta\boldsymbol{x}_1 \\ \Delta\boldsymbol{i}\end{bmatrix} &= \begin{bmatrix}\boldsymbol{A}_4 & \boldsymbol{A}_3 \\ \boldsymbol{A}_2 & \boldsymbol{A}_1\end{bmatrix}\begin{bmatrix}\Delta\boldsymbol{x}_1 \\ \Delta\boldsymbol{i}\end{bmatrix} + \begin{bmatrix}\boldsymbol{B}_2 \\ \boldsymbol{B}_1\end{bmatrix}\Delta\boldsymbol{u}_1 \\ &\quad + \begin{bmatrix}\boldsymbol{C}_2 \\ \boldsymbol{C}_1\end{bmatrix}\Delta\boldsymbol{v} + \begin{bmatrix}\boldsymbol{G}_2 \\ \boldsymbol{G}_1\end{bmatrix}\Delta\boldsymbol{y}_1 \\ \Delta\boldsymbol{m}_1 &= \boldsymbol{H}_2\Delta\boldsymbol{x}_1 + \boldsymbol{H}_1\Delta\boldsymbol{i} + \boldsymbol{F}\Delta\boldsymbol{v} + \boldsymbol{D}\Delta\boldsymbol{u}_1 \\ \Delta\boldsymbol{Y}_1(s) &= G_d(s)\Delta\boldsymbol{M}_1(s) \end{aligned} \tag{4}$$

The involved matrices are computed using a forward finite-difference approach [40] column-by-column, e.g., the $i^{th}$ column of $\boldsymbol{A}_4$ is obtained as follows:

$$\boldsymbol{A}_4^i \approx \frac{\boldsymbol{f}_1(\boldsymbol{x}_1^0 + \epsilon\boldsymbol{I}_n^i, \boldsymbol{i}^0, \boldsymbol{u}_1^0, \boldsymbol{v}^0, \boldsymbol{y}_1^0) - \boldsymbol{f}_1(\boldsymbol{x}_1^0, \boldsymbol{i}^0, \boldsymbol{u}_1^0, \boldsymbol{v}^0, \boldsymbol{y}_1^2)}{\epsilon} \tag{5}$$

The assumed dimensions of the variables are $\boldsymbol{x}_1 \in \mathbb{R}^n$, $\boldsymbol{u}_1 \in \mathbb{R}^k$ and $\boldsymbol{v}, \boldsymbol{i}, \boldsymbol{m}_1, \boldsymbol{y}_1 \in \mathbb{R}^2$; $\boldsymbol{I}_n^i$ is the $i^{th}$ column of an identity matrix of dimension $n$, and $\epsilon$ is a small perturbation parameter. This system can be seen as an hybrid one, where the involved matrices are numerically computed, whereas the delay $G_d(s) = e^{-T_s s}$ is analytically included. From a small-signal perspective, the source subsystem can be thought as either a Thévenin or Norton equivalent. If the former is selected to represent the source subsystem, this can be written as:

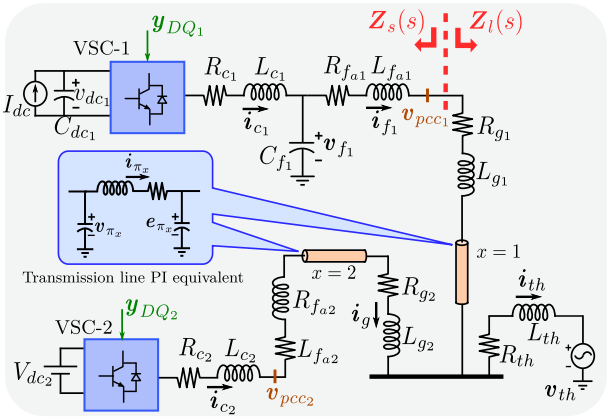


**FIGURE 2.** Test case: Two inverters connected to the grid.

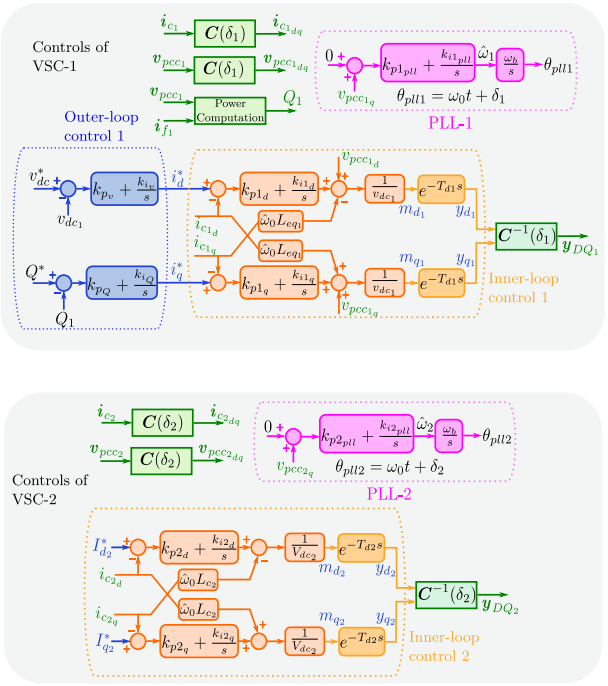


**FIGURE 3.** Controls of the power electronic converters.

$$\boldsymbol{K}_s\Delta\boldsymbol{U}_1(s) = \boldsymbol{Z}_s(s)\Delta\boldsymbol{I}(s) + \Delta\boldsymbol{V}(s) \tag{6}$$

where $\boldsymbol{K}_s$, $\boldsymbol{Z}_s$ are obtained if the state-space model and the algebraic equation in (4) are changed into the frequency domain, and then algebraic manipulations are done using these terms together with the relationship between $\Delta\boldsymbol{Y}_1$ and $\Delta\boldsymbol{M}_1$. This results in:

$$\begin{aligned} \boldsymbol{K} &= (\boldsymbol{A}_2 + \boldsymbol{G}_1 e^{-T_s s}\boldsymbol{H}_2)(s\boldsymbol{I}_n - \boldsymbol{A}_4 - \boldsymbol{G}_2 e^{-T_s s}\boldsymbol{H}_2)^{-1} \\ \boldsymbol{P} &= -\left[\boldsymbol{C}_1 + \boldsymbol{G}_1 e^{-T_s s}\boldsymbol{F} + \boldsymbol{K}(\boldsymbol{C}_2 + \boldsymbol{G}_2 e^{-T_s s}\boldsymbol{F})\right]^{-1} \\ \boldsymbol{Z}_s &= \boldsymbol{P}\left[s\boldsymbol{I}_2 - \boldsymbol{A}_1 - \boldsymbol{G}_1 e^{-T_s s}\boldsymbol{H}_1 - \boldsymbol{K}(\boldsymbol{A}_3 + \boldsymbol{G}_2 e^{-T_s s}\boldsymbol{H}_1)\right] \end{aligned}$$

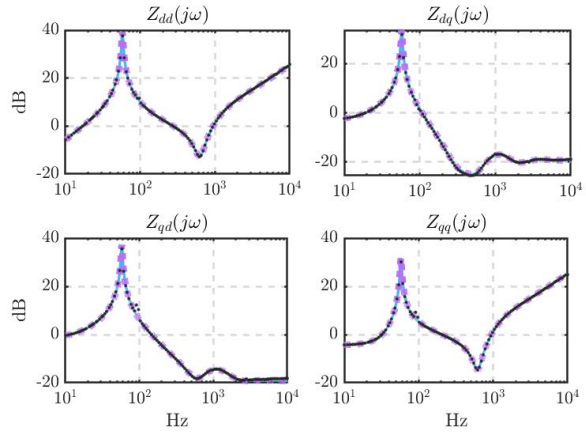


(a) Magnitude $\boldsymbol{Z}_s(j\omega)$

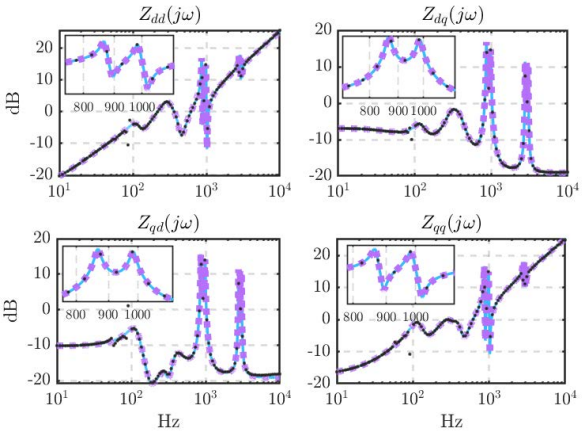


(b) Magnitude $\boldsymbol{Z}_l(j\omega)$

**FIGURE 4.** Impedance models computed with the FDIM-A (–), analytic (- -) and perturbation (·) approaches: weak grid.

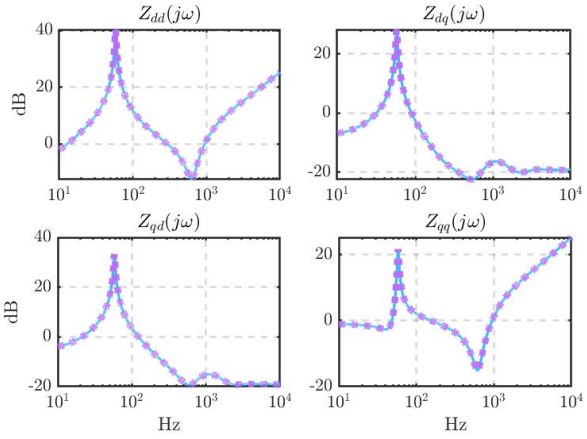


(a) Magnitude $\boldsymbol{Z}_s(j\omega)$

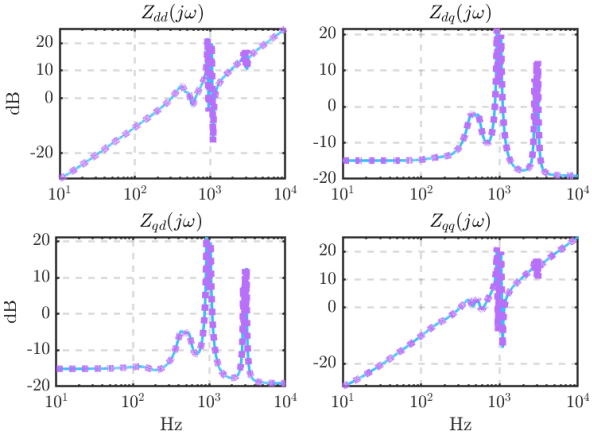


(b) Magnitude $\boldsymbol{Z}_l(j\omega)$

**FIGURE 5.** Impedance models computed with the FDIM-A (–) and the analytic (- -) approaches: stiff grid.

$$\boldsymbol{K}_s = \boldsymbol{P}\left[\boldsymbol{B}_1 + \boldsymbol{G}_1 e^{-T_s s}\boldsymbol{D} + \boldsymbol{K}(\boldsymbol{B}_2 + \boldsymbol{G}_2 e^{-T_s s}\boldsymbol{D})\right] \tag{7}$$

where, $\boldsymbol{I}_n$ and $\boldsymbol{I}_2$ are identity matrices of dimension $n$ and 2, respectively; for brevity, the argument $s$ is omitted. In the case of the load subsystem, a similar derivation can be obtained, it is assumed that its large-signal model is given as follows:

$$\begin{aligned}\frac{d\boldsymbol{i}}{dt} &= \boldsymbol{g}_2(\boldsymbol{x}_2, \boldsymbol{i}, \boldsymbol{u}_2, \boldsymbol{v}, \boldsymbol{y}_2)\\ \frac{d\boldsymbol{x}_2}{dt} &= \boldsymbol{f}_2(\boldsymbol{x}_2, \boldsymbol{i}, \boldsymbol{u}_2, \boldsymbol{v}, \boldsymbol{y}_2)\\ \boldsymbol{m}_2 &= \boldsymbol{q}_2(\boldsymbol{x}_2, \boldsymbol{i}, \boldsymbol{u}_2, \boldsymbol{v})\end{aligned} \tag{8}$$

And the delayed relationship is $\boldsymbol{Y}_2(s) = G_d(s)\boldsymbol{M}_2(s)$, where the delay function $G_d(s)$ can have different delay values of those in the source subsystem. The small-signal model is similarly derived, and a Thévenin equivalent is also selected to represent the load susbsystem:

$$\Delta\boldsymbol{V}(s) = \boldsymbol{Z}_l(s)\Delta\boldsymbol{I}(s) + \boldsymbol{K}_l\Delta\boldsymbol{U}_2(s) \tag{9}$$

The matrices are computed as follows:

$$\begin{aligned}\boldsymbol{K} &= (\boldsymbol{A}_2 + \boldsymbol{G}_1 e^{-T_s s}\boldsymbol{H}_2)(s\boldsymbol{I}_n - \boldsymbol{A}_4 - \boldsymbol{G}_2 e^{-T_s s}\boldsymbol{H}_2)^{-1}\\ \boldsymbol{P} &= \left[\boldsymbol{C}_1 + \boldsymbol{G}_1 e^{-T_s s}\boldsymbol{F} + \boldsymbol{K}(\boldsymbol{C}_2 + \boldsymbol{G}_2 e^{-T_s s}\boldsymbol{F})\right]^{-1}\\ \boldsymbol{Z}_l &= \boldsymbol{P}\left[s\boldsymbol{I}_2 - \boldsymbol{A}_1 - \boldsymbol{G}_1 e^{-T_s s}\boldsymbol{H}_1 - \boldsymbol{K}(\boldsymbol{A}_3 + \boldsymbol{G}_2 e^{-T_s s}\boldsymbol{H}_1)\right]\\ \boldsymbol{K}_l &= -\boldsymbol{P}\left[\boldsymbol{B}_1 + \boldsymbol{G}_1 e^{-T_s s}\boldsymbol{D} + \boldsymbol{K}(\boldsymbol{B}_2 + \boldsymbol{G}_2 e^{-T_s s}\boldsymbol{D})\right]\end{aligned} \tag{10}$$

These expressions lead to the small-signal model regardless of the type of control strategy or system size.

## III. VALIDATION OF THE PROPOSAL

The test case shown in Figure 2 is used to illustrate the proposal. It consists of two power converters interconnected to a grid equivalent through transmission lines that are modeled with a PI equivalent, the system is operating in balanced conditions. The first converter has an LCL passive filter, whereas the second one has an RL filter. The control blocks of both converters are depicted in Figure 3, each VSC is based on typical decoupled current control in the rotating synchronous framework $dq$. The VSC-1 additionally has outer controls that regulate the DC-link voltage and the reactive power. A phase locked loop (PLL) is used to synchronize each converter, and the effect of the PWM and the digital implementation

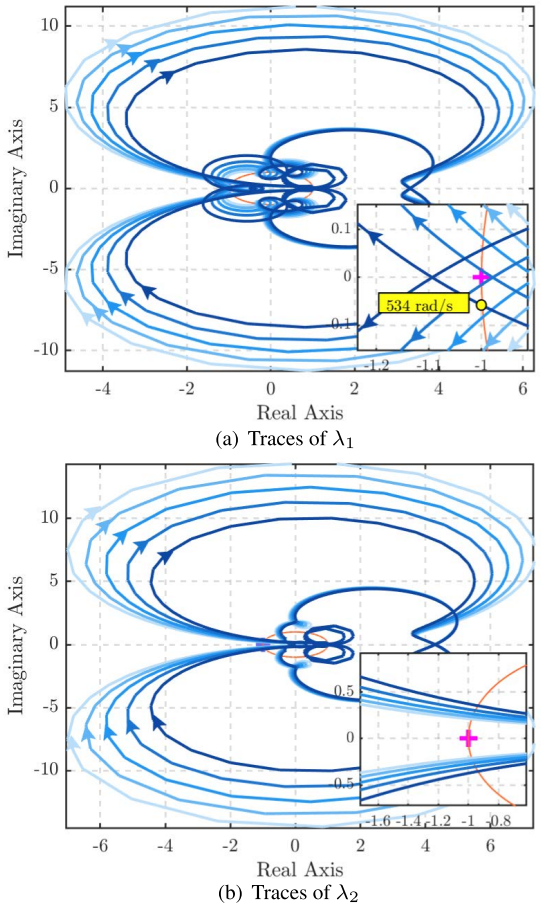


(a) Traces of $\lambda_1$

(b) Traces of $\lambda_2$

**FIGURE 6.** Effect of bandwidth in stability: 1.667 krad/s –, 1.818 krad/s –, 2 krad/s –, 2.222 krad/s –, 2.5 krad/s –.

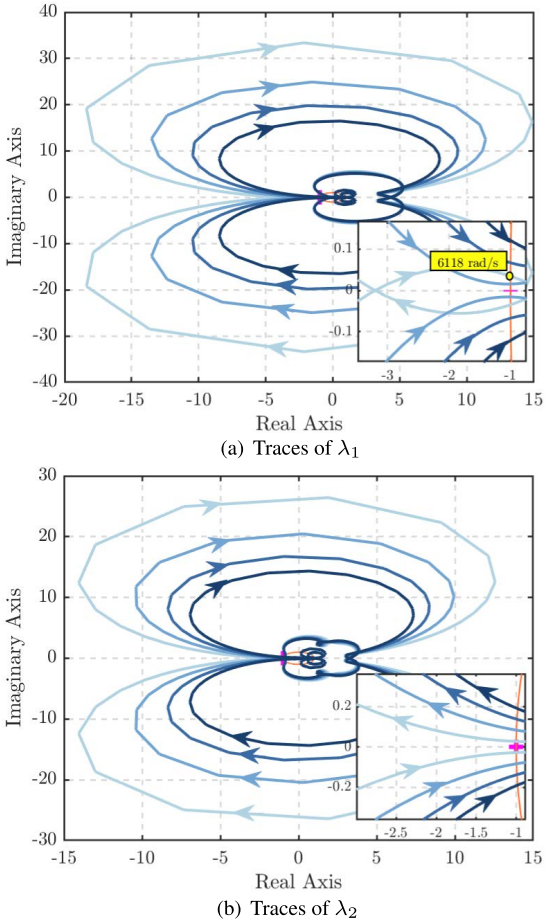


(a) Traces of $\lambda_1$

(b) Traces of $\lambda_2$

**FIGURE 7.** Effect of delay in stability: 198.4 $\mu s$ –, 220 $\mu s$ –, 240 $\mu s$ –, 260 $\mu s$ –.

is represented by the exact delay transfer function. Now, the large-signal model is firstly presented, afterward the numerical linearization is carried out, and then the impedance model is obtained.

### A. LARGE-SIGNAL MODEL

A general frame is used to model all the system elements (this is denoted with capital letters $DQ$), besides there are other two frames oriented with the voltage at the point of common coupling (PCC) $\boldsymbol{v}_{pcc_1}$ and $\boldsymbol{v}_{pcc_2}$ (these are denoted with lowercase $dq$). The PLL gives either the angle $\delta_1$ or $\delta_2$. The knowledge of these angles permits synchronizing each power converter and so, the control strategies can be developed. The change between any of the two frames and the general one can be done using the rotation matrix [41]:

$$\boldsymbol{C}(\delta) = \begin{bmatrix} \cos(\delta) & \sin(\delta) \\ -\sin(\delta) & \cos(\delta) \end{bmatrix} \tag{11}$$

It is worth noting that, due to that the natural framework of the system is into the abc domain, this has to be referred into the $DQ$ frame. This change is accomplished using the Park transform:

$$\boldsymbol{T}(\theta) = \frac{2}{3}\begin{bmatrix} \cos(\theta) & \cos\left(\theta - \frac{2\pi}{3}\right) & \cos\left(\theta + \frac{2\pi}{3}\right) \\ -\sin(\theta) & -\sin\left(\theta - \frac{2\pi}{3}\right) & -\sin\left(\theta + \frac{2\pi}{3}\right) \\ \frac{1}{2} & \frac{1}{2} & \frac{1}{2} \end{bmatrix} \tag{12}$$

where $\theta = \omega_0 t$, being $\omega_0$ the nominal frequency. To study this system, the point of interface between both subsystems is selected at the PCC of the voltage source converter 1 (VSC-1), i.e., $\boldsymbol{v}_{pcc_1}$. Hence, the VSC-1, its controls and the LCL filter are taken as the source subsystem, while the rest of elements are part of the load subsystem. Figure 3 shows the delays represented without rational approximations in both VSCs. First, the state variables of each subsystem are defined according to (3). Then, we have $\boldsymbol{x}_1 = \begin{bmatrix} v_{dc_1} & \delta_1 & x_{pll_1} & x_{d_1} & x_{q_1} & x_{v_1} & x_{Q_1} & \boldsymbol{i}_{c_1} & \boldsymbol{v}_{f_1} \end{bmatrix}^T$, and $\boldsymbol{i}_{c_1} = \begin{bmatrix} i_{c_{1_D}} & i_{c_{1_Q}} \end{bmatrix}^T$, $\boldsymbol{v}_{f_1} = \begin{bmatrix} v_{f_{1_D}} & v_{f_{1_Q}} \end{bmatrix}^T$. The current and voltage in the interface point (in this case results that the interface point is the same that the PCC of VSC-1) are $\boldsymbol{i}_{DQ} = \begin{bmatrix} i_{f_{1_D}} & i_{f_{1_Q}} \end{bmatrix}^T$, $\boldsymbol{v}_{DQ} = \begin{bmatrix} v_{pcc_{1_D}} & v_{pcc_{1_Q}} \end{bmatrix}^T$, respectively; the control references

are $\boldsymbol{u}_1 = \left[v_{dc}^* \; Q^*\right]^T$. The vector $\boldsymbol{x}_1$ contains the integral terms of the proportional integral (pi) controls, the angle phase computed by the PLL, the DC-link voltage and the current and voltage in the LCL filter. The dynamical model in per unit (p.u.) of the source subsystem is as follows: (13), as shown at the bottom of the page, where the most of the variables can be found in Figure 3. Term $\omega_b$ is the base frequency, $\hat{\omega}_0$ is the nominal frequency in p.u., and $L_{eq_1} = L_{c_1} + L_{fa1}$. Due to $\boldsymbol{i}_{c_{1_{dq}}}$, $\boldsymbol{v}_{pcc_{1_{dq}}}$ and $\boldsymbol{y}_{DQ_1}$ are computed using the rotation matrix (11) (see Figure 3), these terms contain nonlinearities that are implicitly in the large-signal model. The voltage $\boldsymbol{v}_{pcc_1}$ is an algebraic variable; however, considering a system with a capacitor in the interface point, this can be a state variable. On the other hand, the large-signal model for the load subsystem is given in (14), as shown at the bottom of the next page.

### B. SMALL-SIGNAL IMPEDANCE MODEL

The parameters of the balanced system are given in Table 1 (the meaning of each parameter is given in the Appendix A) referred to base values of 0.8 MVA, 0.69 kV and 60 Hz; the A-phase of the voltage $\boldsymbol{v}_{th}$ is $1.02\cos(\omega_0 t + 0.11)$ p.u. The results are shown in Figure 4, where the impedance magnitude of both subsystems (in the range 10 Hz-10 kHz) computed with the finite-difference-impedance method with analytical extension (FDIM-A) approach is compared against the perturbation approach whose simulations are carried out in SIMULINK/MATLAB, and analytic expressions (that are given in the Appendix B). The three approaches give similar results and they almost overlap each other, and this permits to validate the proposal. As seen from Table 1, the impedance of the equivalent grid gives a short-circuit ratio (SCR) of 4.5, so this grid is almost weak [42]. Now, it will be considered another operative scenario with a stronger grid with SCR=18 but the same X/R relation. This time, the impedance models are just computed using the analytic and the FDIM-A; the results in Figure 5 show that $\boldsymbol{Z}_s$ is less affected by the impedance of the grid; however, some changes are seen in the main diagonal elements. On the other hand, the grid impedance impacts more the characteristic of the load impedance $\boldsymbol{Z}_l$; the off-diagonal elements seen in Figure 5-(b) have a smaller magnitude in low frequencies compared to 4-(b), moreover, the resonance peaks have bigger values. Regarding to the main diagonal elements, the changes are notable in low frequencies. These results confirm that the proposal correctly identifies weak or stiff systems.

### C. NYQUIST STABILITY ANALYSIS

Checking the stability is a major concern because the system can be undergone to parametric changes. Therefore, is vital to understand how these changes impact in the stable behavior of the system. This task is generally carried out using the generalized Nyquist stability criterion (GNSC) [43]; with the traces of the eigenvalues $\lambda_1(j\omega)$ and $\lambda_2(j\omega)$ of the open-loop gain $\boldsymbol{L}(j\omega) = \boldsymbol{Z}_l(j\omega)\boldsymbol{Z}_s^{-1}(j\omega)$. To verify that the FDIM-A is able to retain the stability properties of the system, it is assessed the sensitivity of the system to changes in the gains of the inner-loop control. The bandwidth of the current control in VSC-2 is varied to find its effect in the stability. The traces of $\lambda_1$ and $\lambda_2$ are shown in Figure 6 using the FDIM-A. Initially, the control is tuned to have a bandwidth of 1.667 krad/s and neither $\lambda_1$ nor $\lambda_2$ encircles the critical point (-1,0). As the bandwidth increases the traces of $\lambda_1$ get closer and closer, and eventually, with a bandwidth of 2.5 krad/s the (-1,0) point is encircled. The system is unstable, and the unstable oscillations are found around 84.988 Hz.

$$
\begin{aligned}
\frac{d}{dt}\begin{bmatrix} v_{dc_1} \\ \delta_1 \\ x_{pll_1} \\ x_{d_1} \\ x_{q_1} \\ x_{v_1} \\ x_{Q_1} \\ i_{c_{1_D}} \\ i_{c_{1_Q}} \\ v_{f_{1_D}} \\ v_{f_{1_Q}} \end{bmatrix} &= \begin{bmatrix} \frac{\omega_b}{C_{dc_1}}\left(I_{dc} - y_{D_1} i_{c_{1_D}} - y_{Q_1} i_{c_{1_Q}}\right) \\ \omega_b(\hat{\omega}_1 - 1) \\ k_{i1_{pll}} v_{pcc_{1_q}} \\ k_{i1_d}(i_d^* - i_{c_{1_d}}) \\ k_{i1_q}(i_q^* - i_{c_{1_q}}) \\ k_{i_v}(v_{dc}^* - v_{dc_1}) \\ k_{i_Q}(Q^* - Q_1) \\ \frac{\omega_b}{L_{c_1}}(v_{dc_1} y_{D_1} - R_{c_1} i_{c_{1_D}} + L_{c_1}\hat{\omega}_0 i_{c_{1_Q}} - v_{f_{1_D}}) \\ \frac{\omega_b}{L_{c_1}}(v_{dc_1} y_{Q_1} - R_{c_1} i_{c_{1_Q}} - L_{c_1}\hat{\omega}_0 i_{c_{1_D}} - v_{f_{1_Q}}) \\ \frac{\omega_b}{C_{f_1}}(i_{c_{1_D}} - i_{f_{1_D}} + C_{f_1}\hat{\omega}_0 v_{f_{1_Q}}) \\ \frac{\omega_b}{C_{f_1}}(i_{c_{1_Q}} - i_{f_{1_Q}} - C_{f_1}\hat{\omega}_0 v_{f_{1_D}}) \end{bmatrix} \\
\frac{d}{dt}\begin{bmatrix} i_{f_{1_D}} \\ i_{f_{1_Q}} \end{bmatrix} &= \frac{\omega_b}{L_{fa1}}\begin{bmatrix} v_{f_{1_D}} - R_{fa1} i_{f_{1_D}} + \hat{\omega}_0 L_{fa1} i_{f_{1_Q}} - v_{pcc_{1_D}} \\ v_{f_{1_Q}} - R_{fa1} i_{f_{1_Q}} - \hat{\omega}_0 L_{fa1} i_{f_{1_D}} - v_{pcc_{1_Q}} \end{bmatrix} \\
\begin{bmatrix} m_{d_1} \\ m_{q_1} \end{bmatrix} &= \frac{1}{v_{dc_1}}\begin{bmatrix} k_{p1_d}(i_d^* - i_{c_{1_d}}) + x_{d_1} - \hat{\omega}_0 L_{eq_1} i_{c_{1_q}} + v_{pcc_{1_d}} \\ k_{p1_q}(i_q^* - i_{c_{1_q}}) + x_{q_1} + \hat{\omega}_0 L_{eq1} i_{c_{1_d}} + v_{pcc_{1_q}} \end{bmatrix} \\
\begin{bmatrix} \Delta Y_{d_1}(s) \\ \Delta Y_{q_1}(s) \end{bmatrix} &= e^{-T_{d1}s}\begin{bmatrix} \Delta M_{d_1}(s) \\ \Delta M_{q_1}(s) \end{bmatrix}
\end{aligned}
\tag{13}
$$

On the other hand, the stability of the scenario with a stiff grid is also assessed. Reducing the bandwidth of the current control in VSC-2 to the value of 1.667 krad/s does not cause instability. So, this time it will be tested the impact of the delay in VSC-2. Initially, $T_{d2} = 198.4\ \mu s$ and neither $\lambda_1$ nor $\lambda_2$ encircle the critical point. Afterward, the delay increases and the Nyquist traces of $\lambda_1$ and $\lambda_2$ are shown in Figure 7. Checking the trace of $\lambda_1$, is seen that the system loses stability for a delay of 260 $\mu s$, expecting that the frequency of the unstable oscillations be around of 973.7 Hz.

Time-domain simulations using the nonlinear model are carried out with SIMULINK to reinforce the outcomes obtained with the FDIM-A. Figure 8 shows that increasing the bandwidth of current control in VSC-2 the system effectively causes oscillations of 85.22 Hz; Regarding to the delay, in Figure 9 is seen that a value of 260 $\mu s$ drives the system to present oscillations of 970 Hz. Both Figures match with high accuracy regarding to the results of the proposal, so this confirms that the FDIM-A retains the stability properties of the system, and can be trustfully used in small-signal studies.

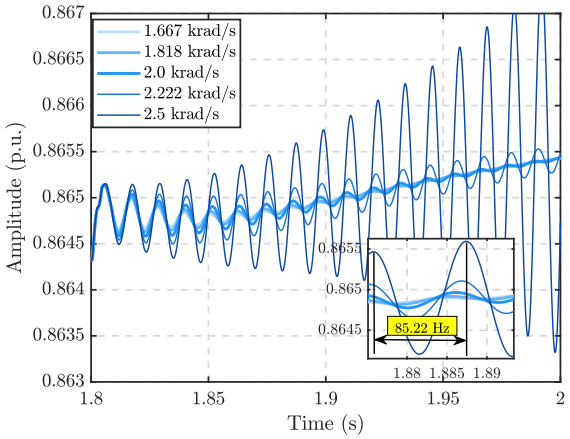


**FIGURE 8.** Response of $i_{f_{1_D}}$ to a step change in $Q^*$ using several bandwidths.

### D. NUMERICAL LAPLACE TRANSFORM STABILITY ANALYSIS

An alternative approach for assessing stability is to get the time-domian waveforms of the system from the impedances

$$
\begin{aligned}
\frac{d}{dt}\begin{bmatrix} i_{f_{1_D}} \\ i_{f_{1_Q}} \end{bmatrix} &= \frac{\omega_b}{L_{g_1}}\begin{bmatrix} v_{pcc_{1_D}} - R_{g_1} i_{f_{1_D}} + \hat{\omega}_0 L_{g_1} i_{f_{1_Q}} - v_{\pi_{1_D}} \\ v_{pcc_{1_Q}} - R_{g_1} i_{f_{1_Q}} - \hat{\omega}_0 L_{g_1} i_{f_{1_D}} v_{\pi_{1_Q}} \end{bmatrix} \\
\frac{d}{dt}\begin{bmatrix} v_{\pi_{1_D}} \\ v_{\pi_{1_Q}} \\ i_{\pi_{1_D}} \\ i_{\pi_{1_Q}} \\ e_{\pi_{1_D}} \\ e_{\pi_{1_Q}} \\ \delta_2 \\ x_{pll_2} \\ x_{d_2} \\ x_{q_2} \\ i_{c_{2_D}} \\ i_{c_{2_Q}} \\ v_{\pi_{2_D}} \\ v_{\pi_{2_Q}} \\ i_{\pi_{2_D}} \\ i_{\pi_{2_Q}} \\ e_{\pi_{2_D}} \\ e_{\pi_{2_Q}} \\ i_{g_D} \\ i_{g_Q} \\ i_{th_D} \\ i_{th_Q} \end{bmatrix} &= \begin{bmatrix} (2\omega_b/C_{\pi_1})(i_{f_{1_D}} - i_{\pi_{1_D}} + \hat{\omega}_0 (C_{\pi_1}/2) v_{\pi_{1_Q}}) \\ (2\omega_b/C_{\pi_1})(i_{f_{1_Q}} - i_{\pi_{1_Q}} - \hat{\omega}_0 (C_{\pi_1}/2) v_{\pi_{1_D}}) \\ (\omega_b/L_{\pi_1})(v_{\pi_{1_D}} - R_{\pi_1} i_{\pi_{1_D}} + \hat{\omega}_0 L_{\pi_1} i_{\pi_{1_Q}} - e_{\pi_{1_D}}) \\ (\omega_b/L_{\pi_1})(v_{\pi_{1_Q}} - R_{\pi_1} i_{\pi_{1_Q}} - \hat{\omega}_0 L_{\pi_1} i_{\pi_{1_D}} - e_{\pi_{1_Q}}) \\ (2\omega_b/C_{\pi_1})(i_{\pi_{1_D}} - i_{th_D} + i_{g_D} + \hat{\omega}_0 (C_{\pi_1}/2) e_{\pi_{1_Q}}) \\ (2\omega_b/C_{\pi_1})(i_{\pi_{1_Q}} - i_{th_Q} + i_{g_Q} - \hat{\omega}_0 (C_{\pi_1}/2) e_{\pi_{1_D}}) \\ \omega_b(\hat{\omega}_2 - 1) \\ k_{i2_{pll}} v_{pcc_{2_q}} \\ k_{i2_d}(I^*_{d_2} - i_{c_{2_d}}) \\ k_{i2_q}(I^*_{q_2} - i_{c_{2_q}}) \\ (\omega_b/L_{eq_2})(V_{dc_2} y_{D_2} - R_{eq_2} i_{c_{2_D}} + \hat{\omega}_0 L_{eq_2} i_{c_{2_Q}} - v_{\pi_{2_D}}) \\ (\omega_b/L_{eq_2})(V_{dc_2} y_{Q_2} - R_{eq_2} i_{c_{2_Q}} - \hat{\omega}_0 L_{eq_2} i_{c_{2_D}} - v_{\pi_{2_Q}}) \\ (2\omega_b/C_{\pi_2})(i_{c_{2_D}} - i_{\pi_{2_D}} + \hat{\omega}_0 (C_{\pi_2}/2) v_{\pi_{2_Q}}) \\ (2\omega_b/C_{\pi_2})(i_{c_{2_Q}} - i_{\pi_{2_Q}} - \hat{\omega}_0 (C_{\pi_2}/2) v_{\pi_{2_D}}) \\ (\omega_b/L_{\pi_2})(v_{\pi_{2_D}} - R_{\pi_2} i_{\pi_{2_D}} + \hat{\omega}_0 L_{\pi_2} i_{\pi_{2_Q}} - e_{\pi_{2_D}}) \\ (\omega_b/L_{\pi_2})(v_{\pi_{2_Q}} - R_{\pi_2} i_{\pi_{2_Q}} - \hat{\omega}_0 L_{\pi_2} i_{\pi_{2_D}} - e_{\pi_{2_Q}}) \\ (2\omega_b/C_{\pi_2})(i_{\pi_{2_D}} - i_{g_D} + \hat{\omega}_0 (C_{\pi_2}/2) e_{\pi_{2_Q}}) \\ (2\omega_b/C_{\pi_2})(i_{\pi_{2_Q}} - i_{g_Q} - \hat{\omega}_0 (C_{\pi_2}/2) e_{\pi_{2_D}}) \\ (\omega_b/L_{g_2})(e_{\pi_{2_D}} - R_{g_2} i_{g_D} + \hat{\omega}_0 L_{g_2} i_{g_Q} - e_{\pi_{1_D}}) \\ (\omega_b/L_{g_2})(e_{\pi_{2_Q}} - R_{g_2} i_{g_Q} - \hat{\omega}_0 L_{g_2} i_{g_D} - e_{\pi_{1_Q}}) \\ (\omega_b/L_{th})(e_{\pi_{1_D}} - R_{th} i_{th_D} + \hat{\omega}_0 L_{th} i_{g_Q} - v_{th_D}) \\ (\omega_b/L_{th})(e_{\pi_{1_Q}} - R_{th} i_{th_Q} - \hat{\omega}_0 L_{th} i_{g_D} - v_{th_Q}) \end{bmatrix} \\
\begin{bmatrix} m_{d_2} \\ m_{q_2} \end{bmatrix} &= \frac{1}{V_{dc_2}}\begin{bmatrix} k_{p2_d}(I^*_{d_2} - i_{c_{2_d}}) + x_{d_2} - \hat{\omega}_0 L_{c_2} i_{c_{2_q}} \\ k_{p2_q}(I^*_{q_2} - i_{c_{2_q}}) + x_{q_2} + \hat{\omega}_0 L_{c_2} i_{c_{2_d}} \end{bmatrix} \\
\begin{bmatrix} \Delta Y_{d_2}(s) \\ \Delta Y_{q_2}(s) \end{bmatrix} &= e^{-T_{d2}s}\begin{bmatrix} \Delta M_{d_2}(s) \\ \Delta M_{q_2}(s) \end{bmatrix}
\end{aligned}
\tag{14}
$$

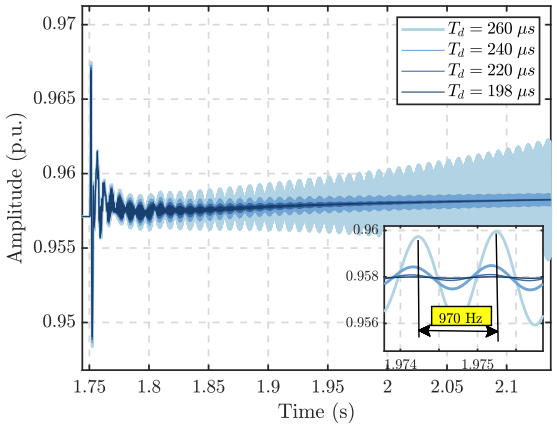


**FIGURE 9.** Response of $i_{f_{1_D}}$ to a step change in $I^*_{q_2}$ for several delays.

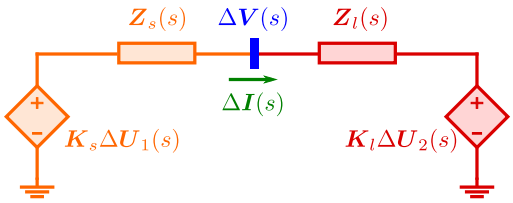


**FIGURE 10.** Small-signal equivalent electric circuit of the test case.

$\boldsymbol{Z}_s(s)$ and $\boldsymbol{Z}_l(s)$ instead of resorting to software such as PSCAD, EMTP-RV or SIMULINK, among others. The conversion from frequency domain to time domain can be conducted through the numerical Laplace transform (NLT) [44], [45], [46], which is a useful tool in the electromagnetic transient (EMT) community, that allows benefits such as accuracy, simplicity and numerical efficiency.

From a small-signal perspective, the test system is represented as Figure 10 indicates, using Thévenin equivalents from both subsystems. The voltage sources represent small perturbations (such as small changes in control references) that can occur in each subsystem. Then, the current or the voltage in the PCC can be computed using basic electric circuit laws. Applying the Kirchhoff's second law to the circuit in Figure 10, leads to the following equation:

$$-\boldsymbol{K}_s \Delta \boldsymbol{U}_1(s) + [\boldsymbol{Z}_s(s) + \boldsymbol{Z}_l(s)]\, \Delta \boldsymbol{I}(s) + \boldsymbol{K}_l \Delta \boldsymbol{U}_2(s) = \boldsymbol{0} \tag{15}$$

and the current is easily obtained as follows:

$$\Delta \boldsymbol{I}(s) = [\boldsymbol{Z}_s(s) + \boldsymbol{Z}_l(s)]^{-1} \left[\boldsymbol{K}_s \Delta \boldsymbol{U}_1(s) - \boldsymbol{K}_l \Delta \boldsymbol{U}_2(s)\right] \tag{16}$$

To demonstrate the effectiveness of the NLT, the small-signal model (16) is solved considering just an occurrence of a slight change of reference in $Q^*$ from 0.1 to 0.11 p.u. This is represented with $\Delta \boldsymbol{U}_1(s) = \left[0\ 0.01/s\right]^T$ and setting $\Delta \boldsymbol{U}_2(s) = \boldsymbol{0}$. The NLT is compared against SIMULINK in Figure 11, where the variable $i_{f_{1_D}} = \Delta i_{f_{1_D}} + i^0_{f_{1_D}}$ is simulated for several bandwidths. Initially, the system is operating in an stable

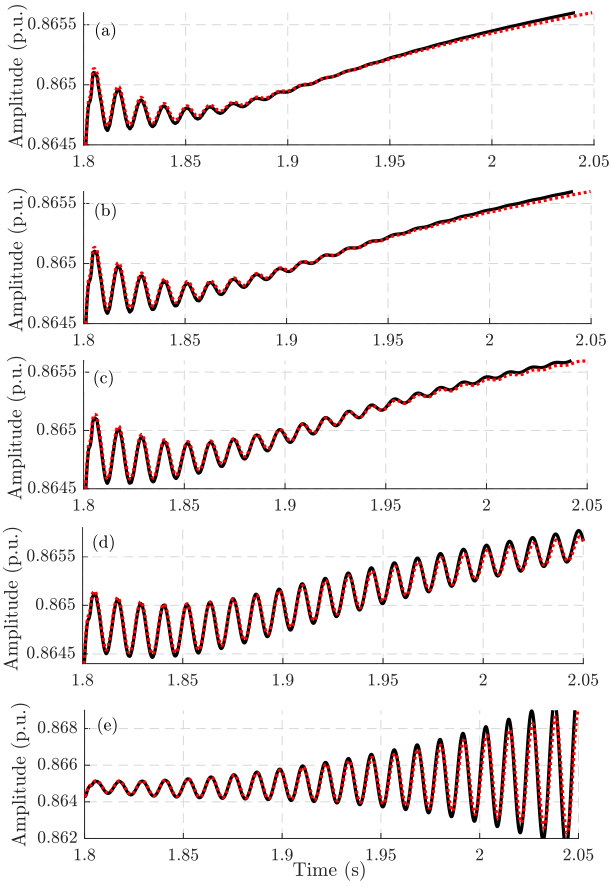


**FIGURE 11.** Current $i_{f_{1_D}}$ using NLT – and SIMULINK ···. Bandwidths: (a) 1.667 krad/s, (b) 1.818 krad/s, (c) 2.0 krad/s, (d) 2.222 krad/s, (e) 2.5 krad/s.

condition; eventually, when the bandwidth is 2.5 krad/s the system presents growing oscillations that are well replicated by the generalized Nyquist stability criterion. The NLT in this case is a useful tool for visualizing the dynamic behavior of the system along with its steady state and also to evaluate the stability as an alternative and complement to Nyquist and Bode diagrams; providing truly waveforms of variables, but with less computational burden in comparison to EMT-software. Moreover, using the NLT to assess the stability does not need to count the encirclements around the point $(-1,0)$ by the Nyquist diagrams. This task can be very difficult, especially when the Nyquist diagrams are complicated draws. This is more notorious in cases where the impedance of any subsystem has several resonance peaks, such as those systems where the long lines models are incorporated into the analysis to take into account the high frequency effects of these elements [44].

## IV. CONCLUSION

This paper has presented an improvement to the finite-difference-impedance method, which permits incorporating the pure delay effect into the impedance model without rational approximations. The method is entirely numerical

**TABLE 1. Parameters of the test case.**

| Parameter | Value | Parameter | Value |
|---|---|---|---|
| $R_{c_1}$ | 0.008 p.u. | $L_{c_1}$ | 0.18 p.u. |
| $C_{f_1}$ | 0.15 p.u. | $R_{f_{a1}}$ | 0.006 p.u. |
| $L_{f_{a1}}$ | 0.11 p.u. | $R_{g_1}$ | 0.006 p.u. |
| $L_{g_1}$ | 0.11 p.u. | $C_{\pi_1}$ | 0.1736 p.u. |
| $L_{\pi_1}$ | 0.0104 p.u. | $R_{\pi_1}$ | 0.004 p.u. |
| $k_{p1_{pll}}$ | 3 p.u. | $k_{i1_{pll}}$ | 120 p.u./s |
| $k_{p1_d}$ | 0.9615 p.u. | $k_{i1_d}$ | 17.5 p.u./s |
| $k_{p1_q}$ | 0.9615 p.u. | $k_{i1_q}$ | 17.5 p.u./s |
| $k_{p_v}$ | -2.182 p.u. | $k_{i_v}$ | -28.37 p.u./s |
| $k_{p_Q}$ | -0.1 p.u. | $k_{i_Q}$ | -2.5 p.u./s |
| $I_{dc}$ | 0.8 p.u. | $C_{dc_1}$ | 8 p.u. |
| $v^*_{dc}$ | 1.3 p.u. | $Q^*$ | 0.1 p.u. |
| $T_{d1}$ | 181.159 $\mu$s | $T_{d2}$ | 198.412 $\mu$s |
| $R_{c_2}$ | 0.005 p.u. | $L_{c_2}$ | 0.12 p.u. |
| $R_{f_{a2}}$ | 0.002 p.u. | $L_{f_{a2}}$ | 0.08 p.u. |
| $C_{\pi_2}$ | 0.1736 p.u. | $L_{\pi_2}$ | 0.0104 p.u. |
| $R_{\pi_2}$ | 0.004 p.u. | $R_{g_2}$ | 0.001 p.u. |
| $L_{g_2}$ | 0.05 p.u. | $k_{p2_{pll}}$ | 4 p.u. |
| $k_{i2_{pll}}$ | 90 p.u./s | $k_{p2_d}$ | 0.53051 p.u. |
| $k_{i2_d}$ | 8.333 p.u./s | $k_{p2_q}$ | 0.53051 p.u. |
| $k_{i2_q}$ | 8.333 p.u./s | $V_{dc_2}$ | 1.1 p.u. |
| $I^*_{d_2}$ | 0.6 p.u. | $I^*_{q_2}$ | 0.1 p.u. |
| $R_{th}$ | 0.03 p.u. | $L_{th}$ | 0.22 p.u. |

oriented, and the only analytic term is related to the exponential term; therefore, the proposal helps to reduce the tedious task of deriving small-signal impedance models of power electronics, especially when larger systems are of interest. The correctness of the method was verified using the traditional analytic and perturbation approaches. Moreover, the NLT was also used to obtain the time-domain response and corroborate the results. The stability assessment showed that the proposal can provide precise and fast information related to oscillatory issues in power electronics-dominated power systems.

## APPENDIX

### A. SYMBOLS DEFINITION

The meaning of each symbol shown in Table 1 is provided here. Where the $x$ stands, it relates to parameters of the VSC-1 ($x = 1$) or VSC-2 ($x = 2$).

- $R_{c_x}$: Resistance of the passive filter in the VSC-side.
- $L_{c_x}$: Inductance of the passive filter in the VSC-side.
- $C_{f_1}$: Capacitance of the passive filter in VSC-1.
- $R_{f_{a_x}}$: Resistance of the passive filter in the grid-side.
- $L_{f_{a_x}}$: Inductance of the passive filter in the grid-side.
- $R_{g_x}$: Resistance of the feeder.
- $L_{g_x}$: Inductance of the feeder.
- $C_{\pi_x}$: Capacitance of the PI equivalent line.
- $R_{\pi_x}$: Resistance of the PI equivalent line.
- $L_{\pi_x}$: Inductance of the PI equivalent line.
- $k_{px_{pll}}$: Proportional gain of the PLL.
- $k_{ix_{pll}}$: Integral gain of the PLL.
- $k_{px_d}$: Proportional gain of the inner loop control for the $d$-current.
- $k_{ix_d}$: Integral gain of the inner loop control for the $d$-current.
- $k_{px_q}$: Proportional gain of the inner loop control for the $q$-current.
- $k_{ix_q}$: Integral gain of the inner loop control for the $q$-current.
- $T_{dx}$: Time delay representing the digital implementation of control and PWM effect.
- $k_{p_v}$: Proportional gain of the outer inner control for the DC-voltage in VSC-1.
- $k_{i_v}$: Integral gain of the outer inner control for the DC-voltage in VSC-1.
- $k_{p_Q}$: Proportional gain of the outer inner control for the reactive power in VSC-1.
- $k_{i_Q}$: Integral gain of the outer inner control for the reactive power in VSC-1.
- $v^*_{dc}$: Control reference of the DC-voltage in VSC-1.
- $Q^*$: Control reference of the reactive power in VSC-1.
- $I^*_{d_2}$: Control reference of the $d$-current in VSC-2.
- $I^*_{q_2}$: Control reference of the $q$-current in VSC-2.
- $R_{th}$: Resistance of the grid equivalent.
- $L_{th}$: Inductance of the grid equivalent.

### B. ANALYTIC IMPEDANCE MODELS

The models are given here, the steady-state value of variables is denoted with uppercase fonts and superindex 0.

- The impedance $\boldsymbol{Z}_s$ of the source subsystem is computed as follows:

$$\boldsymbol{G}_{pll} = \frac{\omega_b}{s}\begin{bmatrix} 0 & \frac{k_{p1_{pll}}s+k_{i1_{pll}}}{s} \end{bmatrix}$$

$$\boldsymbol{G}_b = \left(1 - \boldsymbol{G}_{pll}\frac{\partial \boldsymbol{C}}{\partial \delta_1}\bigg|_{\delta_1^0} \boldsymbol{V}^0_{pcc_1}\right)^{-1} \boldsymbol{G}_{pll}\boldsymbol{C}(\delta_1^0)$$

$$\boldsymbol{K}_i = \begin{bmatrix} -I^0_{f_{1_Q}} & I^0_{f_{1_D}} \end{bmatrix}$$

$$\boldsymbol{K}_v = \begin{bmatrix} V^0_{pcc_{1_Q}} & -V^0_{pcc_{1_D}} \end{bmatrix}$$

$$\boldsymbol{C}_{vdc} = -\begin{bmatrix} \frac{k_{p_v}s+k_{i_v}}{s} & 0 \end{bmatrix}^T$$

$$\boldsymbol{C}_q = -\begin{bmatrix} 0 & \frac{k_{p_Q}s+k_{i_Q}}{s} \end{bmatrix}^T$$

$$\boldsymbol{C}_i = \begin{bmatrix} \frac{k_{p1_d}s+k_{i1_d}}{s} & 0 \\ 0 & \frac{k_{p1_q}s+k_{i1_q}}{s} \end{bmatrix}$$

$$\boldsymbol{G}_{dec} = \begin{bmatrix} 0 & -\hat{\omega}_0 L_{eq_1} \\ \hat{\omega}_0 L_{eq_1} & 0 \end{bmatrix}$$

$$\boldsymbol{\mathcal{A}}_1 = \boldsymbol{C}_i\boldsymbol{C}_q\boldsymbol{K}_i + (\boldsymbol{G}_{dec} - \boldsymbol{C}_i)\frac{\partial \boldsymbol{C}}{\partial \delta_1}\bigg|_{\delta_1^0} \boldsymbol{I}^0_{c_1}\boldsymbol{G}_b + \boldsymbol{C}(\delta_1^0) + \frac{\partial \boldsymbol{C}}{\partial \delta_1}\bigg|_{\delta_1^0} \boldsymbol{V}^0_{pcc_1}\boldsymbol{G}_b$$

$$\boldsymbol{G}_{vpcc} = \frac{e^{-T_{d_1}s}}{V^0_{dc_1}}\boldsymbol{C}^{-1}(\delta_1^0)\boldsymbol{\mathcal{A}}_1 + \frac{\partial \boldsymbol{C}^{-1}}{\partial \delta_1}\bigg|_{\delta_1^0} \boldsymbol{Y}^0_1\boldsymbol{G}_b$$

$$\boldsymbol{G}_{sdq} = \boldsymbol{I}_2 + \frac{\omega_b e^{-T_{d_1}s}}{V^0_{dc_1}C_{dc_1}s}\boldsymbol{C}^{-1}(\delta_1^0)\left(\boldsymbol{C}_i\boldsymbol{C}_{vdc} - \boldsymbol{M}^0_1\right)(\boldsymbol{I}^0_{c_1})^T$$

$$\boldsymbol{\mathcal{A}}_2 = (\boldsymbol{G}_{dec} - \boldsymbol{C}_i)\boldsymbol{C}(\delta_1^0)$$

$$
\begin{aligned}
&- \frac{\omega_b}{C_{dc_1} s}(\boldsymbol{C}_i \boldsymbol{C}_{vdc} - \boldsymbol{M}_1^0)(\boldsymbol{Y}_{DQ_1}^0)^T \\
\boldsymbol{G}_{ic1} &= \frac{e^{-T_{d_1} s}}{V_{dc_1}^0} \boldsymbol{C}^{-1}(\delta_1^0) \boldsymbol{\mathcal{A}}_2 \\
\boldsymbol{G}_{if1} &= \frac{e^{-T_{d_1} s}}{V_{dc_1}^0} \boldsymbol{C}^{-1}(\delta_1^0) \boldsymbol{C}_i \boldsymbol{C}_q \boldsymbol{K}_v \\
\boldsymbol{H}_{sdq} &= V_{dc_1}^0 \boldsymbol{I}_{2\times 2} - \frac{\omega_b}{C_{dc_1} s} \boldsymbol{Y}_{DQ_1}^0 (\boldsymbol{I}_{c_1}^0)^T \\
\boldsymbol{Z}_{c_1} &= \begin{bmatrix} \frac{L_{c_1}}{\omega_b} s + R_{c_1} & -\hat{\omega}_0 L_{c_1} \\ \hat{\omega}_0 L_{c_1} & \frac{L_{c_1}}{\omega_b} s + R_{c_1} \end{bmatrix} \\
\boldsymbol{Y}_c &= \begin{bmatrix} \frac{C_{f_1}}{\omega_b} s & -\hat{\omega}_0 C_{f_1} \\ \hat{\omega}_0 C_{f_1} & \frac{C_{f_1}}{\omega_b} s \end{bmatrix} \\
\boldsymbol{Z}_{f_1} &= \begin{bmatrix} \frac{L_{fa1}}{\omega_b} s + R_{fa1} & -\hat{\omega}_0 L_{fa1} \\ \hat{\omega}_0 L_{fa1} & \frac{L_{fa1}}{\omega_b} s + R_{fa1} \end{bmatrix} \\
\boldsymbol{H}_{ic1} &= \frac{\omega_b}{C_{dc_1} s} \boldsymbol{Y}_{DQ_1}^0 (\boldsymbol{Y}_{DQ_1}^0)^T + \boldsymbol{Z}_{c_1} \\
\boldsymbol{\mathcal{A}}_3 &= \boldsymbol{H}_{sdq} - (\boldsymbol{Y}_c + \boldsymbol{H}_{ic1}^{-1})^{-1} \boldsymbol{H}_{ic1}^{-1} \boldsymbol{H}_{sdq} \\
\boldsymbol{T}_1 &= \left[ \boldsymbol{G}_{sdq} - \boldsymbol{G}_{ic1} \boldsymbol{H}_{ic1}^{-1} \boldsymbol{\mathcal{A}}_3 \right]^{-1} \\
&\quad \times \left[ \boldsymbol{G}_{if1} + \boldsymbol{G}_{ic1} \boldsymbol{H}_{ic1}^{-1} (\boldsymbol{Y}_c + \boldsymbol{H}_{ic1}^{-1})^{-1} \right] \\
\boldsymbol{T}_2 &= \left[ \boldsymbol{G}_{sdq} - \boldsymbol{G}_{ic1} \boldsymbol{H}_{ic1}^{-1} \boldsymbol{\mathcal{A}}_3 \right]^{-1} \boldsymbol{G}_{vpcc} \\
\boldsymbol{\mathcal{A}}_4 &= \boldsymbol{Z}_{f_1} + (\boldsymbol{Y}_c + \boldsymbol{H}_{ic1}^{-1})^{-1} (\boldsymbol{I}_2 - \boldsymbol{H}_{ic1}^{-1} \boldsymbol{H}_{sdq} \boldsymbol{T}_1) \\
\boldsymbol{Z}_s &= \left[ \boldsymbol{I}_2 - (\boldsymbol{Y}_c + \boldsymbol{H}_{ic1}^{-1})^{-1} \boldsymbol{H}_{ic1}^{-1} \boldsymbol{H}_{sdq} \boldsymbol{T}_2 \right]^{-1} \boldsymbol{\mathcal{A}}_4 \\
\boldsymbol{V}_{pcc_1}^0 &= \begin{bmatrix} V_{pcc_{1_D}}^0 & V_{pcc_{1_Q}}^0 \end{bmatrix}^T \\
\boldsymbol{I}_{c_1}^0 &= \begin{bmatrix} I_{c_{1_D}}^0 & I_{c_{1_Q}}^0 \end{bmatrix}^T \\
\boldsymbol{Y}_1^0 &= \begin{bmatrix} Y_{d_1}^0 & Y_{q_1}^0 \end{bmatrix}^T \\
\boldsymbol{M}_1^0 &= \begin{bmatrix} M_{d_1}^0 & M_{q_1}^0 \end{bmatrix}^T \\
\boldsymbol{Y}_{DQ_1}^0 &= \begin{bmatrix} Y_{D_1}^0 & Y_{Q_1}^0 \end{bmatrix}^T \\
\boldsymbol{I}_2 &= \begin{bmatrix} 1 & 0 \\ 0 & 1 \end{bmatrix}
\end{aligned}
$$

- The impedance $\boldsymbol{Z}_l$ is computed as follows:

$$
\begin{aligned}
\boldsymbol{C}_i &= \begin{bmatrix} \frac{k_{p2_d} s + k_{i2_d}}{s} & 0 \\ 0 & \frac{k_{p2_q} s + k_{i2_q}}{s} \end{bmatrix} \\
\boldsymbol{G}_{dec} &= \begin{bmatrix} 0 & -\hat{\omega}_0 L_{c_2} \\ \hat{\omega}_0 L_{c_2} & 0 \end{bmatrix} \\
\boldsymbol{G}_{pll} &= \frac{\omega_b}{s} \begin{bmatrix} 0 & \frac{k_{p2_{pll}} s + k_{i2_{pll}}}{s} \end{bmatrix} \\
\boldsymbol{G}_a &= \left( 1 - \boldsymbol{G}_{pll} \frac{\partial \boldsymbol{C}}{\partial \delta_1}\bigg|_{\delta_2^0} \boldsymbol{V}_{pcc_2}^0 \right)^{-1} \boldsymbol{G}_{pll} \boldsymbol{C}(\delta_2^0) \\
\boldsymbol{\mathcal{B}}_1 &= \boldsymbol{C}^{-1}(\delta_2^0)(-\boldsymbol{C}_i + \boldsymbol{G}_{dec}) \frac{\partial \boldsymbol{C}}{\partial \delta_1}\bigg|_{\delta_2^0} \boldsymbol{I}_{c_2}^0 \boldsymbol{G}_a \\
\boldsymbol{G}_b &= \frac{e^{-T_{d_2} s}}{V_{dc_2}} \boldsymbol{\mathcal{B}}_1 + \frac{\partial \boldsymbol{C}^{-1}}{\partial \delta_1}\bigg|_{\delta_2^0} \boldsymbol{Y}_2^0 \boldsymbol{G}_a \\
\boldsymbol{Z}_{c_2} &= \begin{bmatrix} \frac{L_{c_2}}{\omega_b} s + R_{c_2} & -\hat{\omega}_0 L_{c_2} \\ \hat{\omega}_0 L_{c_2} & \frac{L_{c_2}}{\omega_b} s + R_{c_2} \end{bmatrix} \\
\boldsymbol{\mathcal{B}}_2 &= e^{-T_{d_2} s} \boldsymbol{C}^{-1}(\delta_2^0)(-\boldsymbol{C}_i + \boldsymbol{G}_{dec}) \boldsymbol{C}(\delta_2^0) \\
\boldsymbol{Z}_{conv_2} &= (\boldsymbol{I}_2 - V_{dc_2} \boldsymbol{G}_b)^{-1} \left[ \boldsymbol{Z}_{c_2} - \boldsymbol{\mathcal{B}}_2 \right] \\
\boldsymbol{Z}_{f_2} &= \begin{bmatrix} \frac{L_{fa2}}{\omega_b} s + R_{fa2} & -\hat{\omega}_0 L_{fa2} \\ \hat{\omega}_0 L_{fa2} & \frac{L_{fa2}}{\omega_b} s + R_{fa2} \end{bmatrix} \\
\boldsymbol{Y}_{2_a} &= \frac{1}{2} \begin{bmatrix} \frac{C_{\pi_2}}{\omega_b} s & -\hat{\omega}_0 C_{\pi_2} \\ \hat{\omega}_0 C_{\pi_2} & \frac{C_{\pi_2}}{\omega_b} s \end{bmatrix} \\
\boldsymbol{Z}_{\pi_2} &= \begin{bmatrix} \frac{L_{\pi_2}}{\omega_b} s + R_{\pi_2} & -\hat{\omega}_0 L_{\pi_2} \\ \hat{\omega}_0 L_{\pi_2} & \frac{L_{\pi_2}}{\omega_b} s + R_{\pi_2} \end{bmatrix} \\
\boldsymbol{Y}_{2_b} &= \frac{1}{2} \begin{bmatrix} \frac{C_{\pi_2}}{\omega_b} s - \hat{\omega}_0 C_{\pi_2} & \\ \hat{\omega}_0 C_{\pi_2} & \frac{C_{\pi_2}}{\omega_b} s \end{bmatrix} \\
\boldsymbol{Z}_{g_2} &= \begin{bmatrix} \frac{L_{g_2}}{\omega_b} s + R_{g_2} & -\hat{\omega}_0 L_{g_2} \\ \hat{\omega}_0 L_{g_2} & \frac{L_{g_2}}{\omega_b} s + R_{g_2} \end{bmatrix} \\
\boldsymbol{Z}_{th} &= \begin{bmatrix} \frac{L_{th}}{\omega_b} s + R_{th} & -\hat{\omega}_0 L_{th} \\ \hat{\omega}_0 L_{th} & \frac{L_{th}}{\omega_b} s + R_{th} \end{bmatrix} \\
\boldsymbol{\mathcal{B}}_3 &= \left[ \boldsymbol{Y}_{2_a} + (\boldsymbol{Z}_{f_2} + \boldsymbol{Z}_{conv_2})^{-1} \right]^{-1} \\
\boldsymbol{Z} &= \boldsymbol{Z}_{g_2} + \left( \boldsymbol{Y}_{2_b} + \left\{ \boldsymbol{Z}_{\pi_2} + \boldsymbol{\mathcal{B}}_3 \right\}^{-1} \right)^{-1} \\
\boldsymbol{Z}_{eq} &= \left( \boldsymbol{Z}^{-1} + \boldsymbol{Z}_{th}^{-1} \right)^{-1} \\
\boldsymbol{Z}_{g_1} &= \begin{bmatrix} \frac{L_{g_1}}{\omega_b} s + R_{g_1} & -\hat{\omega}_0 L_{g_1} \\ \hat{\omega}_0 L_{g_1} & \frac{L_{g_1}}{\omega_b} s + R_{g_1} \end{bmatrix} \\
\boldsymbol{Y}_{1_a} &= \frac{1}{2} \begin{bmatrix} \frac{C_{\pi_1}}{\omega_b} s & -\hat{\omega}_0 C_{\pi_1} \\ \hat{\omega}_0 C_{\pi_1} & \frac{C_{\pi_1}}{\omega_b} s \end{bmatrix} \\
\boldsymbol{Z}_{\pi_1} &= \begin{bmatrix} \frac{L_{\pi_1}}{\omega_b} s + R_{\pi_1} & -\hat{\omega}_0 L_{\pi_1} \\ \hat{\omega}_0 L_{\pi_1} & \frac{L_{\pi_1}}{\omega_b} s + R_{\pi_1} \end{bmatrix} \\
\boldsymbol{Y}_{1_b} &= \frac{1}{2} \begin{bmatrix} \frac{C_{\pi_1}}{\omega_b} s & -\hat{\omega}_0 C_{\pi_1} \\ \hat{\omega}_0 C_{\pi_1} & \frac{C_{\pi_1}}{\omega_b} s \end{bmatrix} \\
\boldsymbol{Z}_l &= \boldsymbol{Z}_{g_1} + \left\{ \boldsymbol{Y}_{1_b} + \left[ \boldsymbol{Z}_{\pi_1} + (\boldsymbol{Y}_{1_b} + \boldsymbol{Z}_{eq}^{-1})^{-1} \right]^{-1} \right\}^{-1} \\
\boldsymbol{V}_{pcc_2}^0 &= \begin{bmatrix} V_{pcc_{2_D}}^0 & V_{pcc_{2_Q}}^0 \end{bmatrix}^T \\
\boldsymbol{I}_{c_2}^0 &= \begin{bmatrix} I_{c_{2_D}}^0 & I_{c_{2_Q}}^0 \end{bmatrix}^T \\
\boldsymbol{Y}_2^0 &= \begin{bmatrix} Y_{d_2}^0 & Y_{q_2}^0 \end{bmatrix}^T
\end{aligned}
$$

## REFERENCES


[1] J. Sun, "Impedance-based stability criterion for grid-connected inverters," *IEEE Trans. Power Electron.*, vol. 26, no. 11, pp. 3075–3078, Nov. 2011.

[2] M. Wang, Z. Cao, B. Liu, J. Li, T. Fernando, and X. Liu, "Impedance modeling and stability analysis of all-DC delivered offshore wind farm," *IEEE J. Emerg. Sel. Topics Circuits Syst.*, vol. 12, no. 1, pp. 20–28, Mar. 2022.

[3] M. Wang, Y. Chen, X. Dong, S. Hu, B. Liu, S. S. Yu, H. Ma, X. Zhang, and X. Liu, "Impedance modeling and stability analysis of DFIG wind farm with LCC-HVDC transmission," *IEEE J. Emerg. Sel. Topics Circuits Syst.*, vol. 12, no. 1, pp. 7–19, Mar. 2022.

[4] W. Wu, M. Zhang, Y. Chen, L. Zhou, A. Luo, X. Zhou, Z. He, L. Yang, Z. Xie, and J. Liu, "Sequence impedance modeling and stability comparative analysis of voltage-controlled VSGs and current-controlled VSGs," *IEEE Trans. Ind. Electron.*, vol. 66, no. 8, pp. 6460–6472, Aug. 2019.

[5] Y. Liu, X. Zhou, H. Yu, L. Hong, H. Xia, H. Yin, Y. Chen, L. Zhou, and W. Wu, "Sequence impedance modeling and stability assessment for load converters in weak grids," *IEEE Trans. Ind. Electron.*, vol. 68, no. 5, pp. 4056–4067, May 2021.

[6] Y. Jiao and H. Nian, "Grid-forming control for DFIG based wind farms to enhance the stability of LCC-HVDC," *IEEE Access*, vol. 8, pp. 156752–156762, 2020.

[7] M. Amin and M. Molinas, "Small-signal stability assessment of power electronics based power systems: A discussion of impedance- and eigenvalue-based methods," *IEEE Trans. Ind. Appl.*, vol. 53, no. 5, pp. 5014–5030, Sep./Oct. 2017.

[8] H. Nian, J. Yang, B. Hu, Y. Jiao, Y. Xu, and M. Li, "Stability analysis and impedance reshaping method for DC resonance in VSCs-based power system," *IEEE Trans. Energy Convers.*, vol. 36, no. 4, pp. 3344–3354, Dec. 2021.

[9] S. Golestan, E. Ebrahimzadeh, B. Wen, J. M. Guerrero, and J. C. Vasquez, "Dq-frame impedance modeling of three-phase grid-tied voltage source converters equipped with advanced PLLs," *IEEE Trans. Power Electron.*, vol. 36, no. 3, pp. 3524–3539, Mar. 2021.

[10] J. Guo, Y. Chen, S. Liao, W. Wu, L. Zhou, Z. Xie, and X. Wang, "Analysis and mitigation of low-frequency interactions between the source and load virtual synchronous machine in an islanded microgrid," *IEEE Trans. Ind. Electron.*, vol. 69, no. 4, pp. 3732–3742, Apr. 2022.

[11] H. Zong, C. Zhang, J. Lyu, X. Cai, M. Molinas, and F. Rao, "Generalized MIMO sequence impedance modeling and stability analysis of MMC-HVDC with wind farm considering frequency couplings," *IEEE Access*, vol. 8, pp. 55602–55618, 2020.

[12] Z. Xu, B. Li, L. Han, J. Hu, S. Wang, S. Zhang, and D. Xu, "A complete HSS-based impedance model of MMC considering grid impedance coupling," *IEEE Trans. Power Electron.*, vol. 35, no. 12, pp. 12929–12948, Dec. 2020.

[13] X. Xiong, Y. Yang, C. Wu, C. Zhao, and F. Blaabjerg, "Improving the stability of standalone MMCs by shaping the AC side impedance using insertion index compensation," *IEEE J. Emerg. Sel. Topics Circuits Syst.*, vol. 12, no. 1, pp. 81–89, Mar. 2022.

[14] C. Zhang, M. Molinas, S. Foyen, J. A. Suul, and T. Isobe, "An integrated method for generating VSCs' periodical steady-state conditions and HSS-based impedance model," *IEEE Trans. Power Del.*, vol. 35, no. 5, pp. 2544–2547, Oct. 2020.

[15] Y. Liao and X. Wang, "Stationary-frame complex-valued frequency-domain modeling of three-phase power converters," *IEEE J. Emerg. Sel. Topics Power Electron.*, vol. 8, no. 2, pp. 1922–1933, Jun. 2020.

[16] H. Tao, H. Hu, X. Zhu, Y. Zhou, and Z. He, "Harmonic instability analysis and suppression method based on $\alpha\beta$-frame impedance for trains and network interaction system," *IEEE Trans. Energy Convers.*, vol. 34, no. 2, pp. 1124–1134, Jun. 2019.

[17] A. Rygg, M. Molinas, C. Zhang, and X. Cai, "A modified sequence-domain impedance definition and its equivalence to the dq-domain impedance definition for the stability analysis of AC power electronic systems," *IEEE J. Emerg. Select. Topics Power Electron.*, vol. 4, no. 4, pp. 1383–1396, Dec. 2016.

[18] S. Zhu, L. Qin, K. Liu, K. Ji, Y. Li, Q. Huai, X. Liao, and S. Yang, "Impedance modeling of modular multilevel converter in D-Q and modified sequence domains," *IEEE J. Emerg. Sel. Topics Power Electron.*, vol. 10, no. 4, pp. 4361–4382, Aug. 2022.

[19] Y. Zhou, H. Hu, J. Yang, and Z. He, "A novel forbidden-region-based stability criterion in modified sequence-domain for AC grid-converter system," *IEEE Trans. Power Electron.*, vol. 34, no. 4, pp. 2988–2995, Apr. 2019.

[20] Y. Tang, R. Burgos, B. Wen, D. Boroyevich, J. Verhulst, D. Vrtachnik, and M. Belkhayat, "A novel DQ impedance measurement method in three-phase balanced systems," in *Proc. 20th Workshop Control Modeling Power Electron. (COMPEL)*, Jun. 2019, pp. 1–5.

[21] Z. Shen, M. Jaksic, P. Mattavelli, D. Boroyevich, J. Verhulst, and M. Belkhayat, "Design and implementation of three-phase AC impedance measurement unit (IMU) with series and shunt injection," in *Proc. 28th Annu. IEEE Appl. Power Electron. Conf. Expo. (APEC)*, Mar. 2013, pp. 2674–2681.

[22] A. Rygg and M. Molinas, "Apparent impedance analysis: A small-signal method for stability analysis of power electronic-based systems," *IEEE J. Emerg. Sel. Topics Power Electron.*, vol. 5, no. 4, pp. 1474–1486, Dec. 2017.

[23] Y. Zhang, X. Du, Y. Shi, C. Zeng, J. Liu, and H.-M. Tai, "Impedance scanning method of grid-tied converters under nonzero grid impedance condition," in *Proc. IEEE 10th Int. Symp. Power Electron. Distrib. Gener. Syst. (PEDG)*, Jun. 2019, pp. 728–733.

[24] T. Roinila, H. Abdollahi, and E. Santi, "Frequency-domain identification based on pseudorandom sequences in analysis and control of DC power distribution systems: A review," *IEEE Trans. Power Electron.*, vol. 36, no. 4, pp. 3744–3756, Apr. 2021.

[25] H. Alenius, R. Luhtala, and T. Roinila, "Combination of orthogonal injections in impedance measurements of grid-connected systems," *IEEE Access*, vol. 8, pp. 178085–178096, 2020.

[26] T. Roinila, T. Messo, and E. Santi, "MIMO-identification techniques for rapid impedance-based stability assessment of three-phase systems in DQ domain," *IEEE Trans. Power Electron.*, vol. 33, no. 5, pp. 4015–4022, May 2018.

[27] A. Riccobono, M. Mirz, and A. Monti, "Noninvasive online parametric identification of three-phase AC power impedances to assess the stability of grid-tied power electronic inverters in LV networks," *IEEE J. Emerg. Sel. Topics Power Electron.*, vol. 6, no. 2, pp. 629–647, Jun. 2018.

[28] M. Ciobotaru, R. Teodorescu, P. Rodriguez, A. Timbus, and F. Blaabjerg, "Online grid impedance estimation for single-phase grid-connected systems using PQ variations," in *Proc. IEEE Power Electron. Specialists Conf.*, 2007, pp. 2306–2312.

[29] N. Mohammed, M. Ciobotaru, and G. Town, "An improved grid impedance estimation technique under unbalanced voltage conditions," in *Proc. IEEE PES Innov. Smart Grid Technol. Eur. (ISGT-Eur.)*, Sep. 2019, pp. 1–5.

[30] J.-H. Cho, K.-Y. Choi, Y.-W. Kim, and R.-Y. Kim, "A novel P-Q variations method using a decoupled injection of reference currents for a precise estimation of grid impedance," in *Proc. IEEE Energy Convers. Congr. Exposit. (ECCE)*, Sep. 2014, pp. 5059–5064.

[31] N. Mohammed, T. Kerekes, and M. Ciobotaru, "An online event-based grid impedance estimation technique using grid-connected inverters," *IEEE Trans. Power Electron.*, vol. 36, no. 5, pp. 6106–6117, May 2021.

[32] M. Zhang, X. Wang, D. Yang, and M. G. Christensen, "Artificial neural network based identification of multi-operating-point impedance model," *IEEE Trans. Power Electron.*, vol. 36, no. 2, pp. 1231–1235, Feb. 2021.

[33] S. Kamala, N. B. Y. Gorla, and S. K. Panda, "Small-signal stability improvement of microgrid with battery energy storage system based on real-time grid impedance measurement," *IEEE Trans. Ind. Appl.*, vol. 58, no. 2, pp. 2537–2546, Mar. 2022.

[34] Y. Xu, M. Zhang, L. Fan, and Z. Miao, "Small-signal stability analysis of type-4 wind in series-compensated networks," *IEEE Trans. Energy Convers.*, vol. 35, no. 1, pp. 529–538, Mar. 2020.

[35] L. Wang, J. Peng, Y. You, and H. Ma, "Iterative approach to impedance model for small-signal stability analysis," *IET Renew. Power Gener.*, vol. 13, no. 1, pp. 78–85, Jan. 2019.

[36] D. D. Giudice, A. Brambilla, D. Linaro, and F. Bizzarri, "Modular multilevel converter impedance computation based on periodic small-signal analysis and vector fitting," *IEEE Trans. Circuits Syst. I, Reg. Papers*, vol. 69, no. 4, pp. 1832–1842, Apr. 2022.

[37] J. Hernández-Ramírez, J. Segundo, F. Martínez-Cárdenas, and P. Gómez, "Linearization of periodic power electronic-based power systems for small-signal analysis," *Int. J. Electr. Power Energy Syst.*, vol. 135, Feb. 2022, Art. no. 107503. [Online]. Available: https://www.sciencedirect.com/science/article/pii/S0142061521007420

[38] J. Ramírez-Hernández, J. Segundo, N. Visairo, and C. Núñez-Guitérrez, "A finite-difference-impedance method for stability analysis of power-electronics-based power system," *Int. J. Electr. Power Energy Syst., Under Rev.*, pp. 1–9, Oct. 2022.

[39] P. De Rua and J. Beerten, "Generalization of harmonic state-space framework to delayed periodic systems for stability analysis of the modular multilevel converter," *IEEE Trans. Power Del.*, vol. 37, no. 4, pp. 2661–2672, Aug. 2022.
[40] J. Nocedal and S. J. Wright, *Numerical Optimization*. New York, NY, USA: Springer, 2006.
[41] N. Pogaku, M. Prodanovic, and T. C. Green, "Modeling, analysis and testing of autonomous operation of an inverter-based microgrid," *IEEE Trans. Power Electron.*, vol. 22, no. 2, pp. 613–625, Mar. 2007.
[42] L. Huang, C. Wu, D. Zhou, and F. Blaabjerg, "Impact of grid strength and impedance characteristics on the maximum power transfer capability of grid-connected inverters," *Appl. Sci.*, vol. 11, no. 9, p. 4288, 2021. [Online]. Available: https://www.mdpi.com/2076-3417/11/9/4288
[43] A. J. Macfarlane, "Multivariable nyquist-bode and multivariable root-locus techniques," in *Proc. IEEE Conf. Decis. Control, 15th Symp. Adapt. Processes*, Dec. 1976, pp. 342–347.
[44] J. Segundo-Ramirez, A. Bayo-Salas, M. Esparza, J. Beerten, and P. Gomez, "Frequency domain methods for accuracy assessment of wideband models in electromagnetic transient stability studies," *IEEE Trans. Power Del.*, vol. 35, no. 1, pp. 71–83, Feb. 2020.
[45] P. Moreno and A. Ramirez, "Implementation of the numerical Laplace transform: A review," *IEEE Trans. Power Del.*, vol. 23, no. 4, pp. 2599–2609, Oct. 2008.
[46] H. A. Alameri and P. Gomez, "Laplace domain modeling of power components for transient converter-grid interaction studies," in *Proc. North Amer. Power Symp. (NAPS)*, Nov. 2021, pp. 1–6.

**JUAN SEGUNDO-RAMÍREZ** (Member, IEEE) received the M.Sc. degree in electrical power systems from Cinvestav Guadalajara, Mexico, in 2004, and the Ph.D. degree in electrical power systems from the Universidad Michoacana de San Nicolas de Hidalgo, Michoacán, Mexico, in 2010. Since 2010, he has been with the Universidad Autónoma de San Luis Potosí, San Luis Potosí, Mexico. His research interests include power system harmonic analysis, modeling, and simulation.

**JULIO HERNÁNDEZ-RAMÍREZ** received the M.Sc. degree in electrical engineering from the Universidad Autónoma de San Luis Potosí, San Luis Potosí, Mexico, in 2017, where he is currently pursuing the Ph.D. degree in electrical engineering. He worked with the Electrical Studies Unit, National Center for Energy Control (CENACE), Mexico City, as a Power System Analyst, from 2018 to 2019. His research interests include modeling of renewable energy systems, stability in power systems with power electronic penetration, and electromagnetic transients.

**NANCY VISAIRO-CRUZ** (Member, IEEE) received the Graduate degree in electronic engineering from the Technologic Institute of Oaxaca, Mexico, in 1997, and the M.S. and Ph.D. degrees in automatic control from the National Center for Research and Technological Development, Cuernavaca, Mexico, in 1999 and 2004, respectively. Since 2005, she has been working as a Professor/ a Researcher with the Center for Research and Graduate Studies, Faculty of Engineering, Autonomous University of San Luis Potosí. She is a member of the National Research System at Level 1. Her research interests include automatic control schemes for power electronics systems applied to power quality, electric vehicles, renewable energy, storage systems, and fault diagnosis topics to energy storage systems.

**C. ALBERTO NÚÑEZ GUITIÉRREZ** received the M.Sc. and Ph.D. degrees from CENIDET, Cuernavaca, in 1997 and 2002, respectively. Since 2002, he has been with the Autonomous University of San Luis Potosí, as a Professor and a Researcher. He has led several research industrial projects with the mining industry, power systems industries, and government. His research interests include power electronics, control of power converters, and power quality.